Equation for the force experienced by a wall overflowed by a granular avalanche: experimental verification

Thierry Faug, P. Caccamo, B. Chanut

Equation for the force experienced by a wall overflowed by a granular avalanche: experimental verification

Thierry Faug* and Paolo Caccamo, Benoit Chanut

Cemagref, ETGR, 38402 St. Martin d'Hères, France

(Dated: September 2011)

Abstract

The present paper deals with the force experienced by a wall overflowed by a granular avalanche. First, we shortly report new laboratory tests on dry granular avalanches overflowing a wall down a rough channel. In the first step, the thickness and velocity of the control flows without a wall are measured. In the second step, a wall is mounted to obstruct the flow and the normal force experienced by the wall is measured. Then, a set of equations based on depth-averaged momentum conservation and making it possible to derive the time-varying force on the wall is described. The model was proposed and calibrated on 2D discrete numerical simulations in an earlier work [B. Chanut, T. Faug, and M. Naaim, Phys. Rev. E 82, 041302 (2010)]. This model takes into account the fact that a quasi-static stagnant zone is established upstream of the wall and coexists with an inertial flowing zone above. For a large range of slopes, the model's prediction is successfully compared to experimental data with a reasonable estimation of the incoming flow density and in spite of some rough assumptions made to describe the dynamics of the dead zone. Finally, the results are analysed with regards to previous 2D discrete numerical simulations and we discuss the future work to be undertaken on the dynamics of the dead zone established upstream of the wall.

*Electronic address: thierry.faug@cemagref.fr

1. INTRODUCTION

Understanding granular flow dynamics around obstacles and the force exerted by the flow on the obstacle is an important question in different fields such as storage and conveying processes in industry [1] or defence structures against geophysical flows [2, 3]. Certain studies have focused on the drag experienced by various objects inside granular flows. The quasi-static regime, from the pioneering work of Wieghardt [4] to more recent studies [5–9], has been investigated. The rapid-dilute regime has been also studied [10–16]. Besides quasi-static (solid) and rapid-dilute (gazeous) regimes, granular flows can exhibit an intermediate dense regime [17] referring to the so-called granular liquid regime [18]. However, the theoretical description of dense-liquid granular flows remains an open question in spite of recent progress [18, 19]. Little attention has been paid to granular force on objects in this intermediate flow regime.

This paper focuses on channelized dense dry granular avalanches overflowing a flat obstacle spanning the channel. The time-varying force on the wall exerted by the free-surface gravity-driven flow is analysed by cross-comparing the new laboratory tests and the prediction of an analytical model based on depth-averaged momentum conservation previously developed for 2D granular flows and calibrated using discrete element method (DEM) numerical simulations [20, 21]. In presence of a large obstacle: a wall spanning the flow, these experiments show the formation of a quasi-static stagnant zone upstream of the wall which co-exists with an inertial zone overflowing the wall: see Fig.1. Importantly is to notice that this flow–obstacle interaction regime, obtained on a rough bed, does not refer to granular jumps outlined earlier for rapid flows on relatively smooth beds [22–25]. By successfully cross-comparing the experimental force to the analytical prediction, this study demonstrates the robustness of the proposed equation to link the growth of the dead zone to the mean resulting force on the wall.

The experimental set-up and procedure to investigate granular avalanches impacting a wall –normal to the incident flow and the bottom– are presented in Sec.2. Section 3 is dedicated to a succinct description of the analytical model (previously reported in detail in [20] for the steady regime and in [21] for the avalanche regime), which aims at predicting the force from a granular avalanche on a wall in presence of a dead zone. Section 4 deals with the cross-comparison between the laboratory data and the model's prediction in term

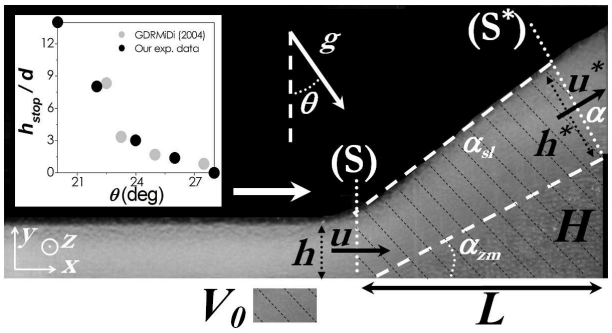

FIG. 1: Granular avalanche overflowing a wall of height $H = 25d$ (example for laboratory tests at $\theta = 31°$): co-existence of a quasi-static stagnant zone and a flowing inertial zone upstream of the wall. The snapshot is the sum of 15 images in order to distinguish the flowing zone and the stagnant zone. Inset: function $h_{stop}(\theta)$.

of the time-varying force on the wall. Finally, the paper is concluded by a discussion on the results and on the prospective work in link with the dead zone dynamics.

2. LABORATORY TESTS

The experimental set-up is a 1.3-m-long and 0.25-m-wide rough (sandpaper) channel mounted on an incline whose slope angle θ can be varied. The channel is equipped with a reservoir to store the granular material released by opening a gate at a constant height $H_0 =$ 3.5 cm. The granular material consists of glass beads (a constant mass, m=9.2 kg, is released for each test) with a mean diameter d =1 mm and a particle density ρ_P=2450 kg m^{-3}. A sketch of the experimental set-up is depicted in Fig.2. The material was characterized by the angles θ_{min}=20°, related to the effective friction associated with quasi-static deformation, and the angle θ_{max}=28° related to rapid collisional flows. These angles were derived from the function $h_{stop}(\theta)$, similarly to the procedure described in [19, 26] (see inset in Fig.1). Two series of experiments were conducted within a large range of slopes, each degree, from 21° (just above θ_{min} for which the avalanche release is prevented) to θ_c =33°, relatively larger than θ_{max}.

Control avalanche flows –in absence of the wall– were first studied. The time-varying flow thickness $h(t)$ was measured at the distance x_0/d=1300 from the gate (channel exit) using a laser sheet deflected by the granular mass and a high-speed video camera recording

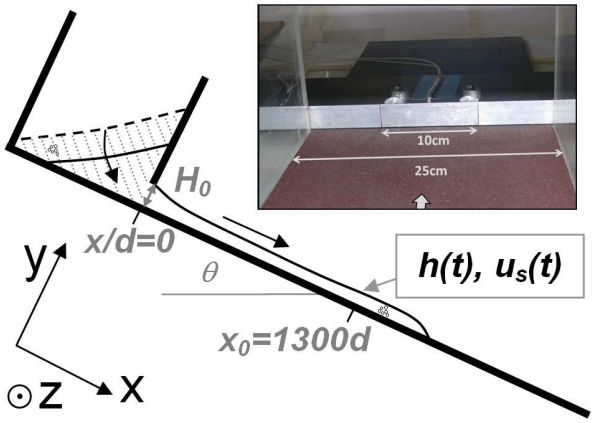

FIG. 2: Sketch of the experimental set-up. A finite volume hatched area of an assembly of beads (mean diameter d) is suddenly released from the reservoir by an aperture of height $H_0 = 35d$, and the grains flow down the inclined slope. In inset is shown the wall spanning the flow: only the ten central centimeters, over the 25-cm width of the channel, were connected to the two force sensors (the white arrow indicates the avalanche flow direction).

the images from 200 to 350 fps depending on the slope inclination. The surface velocity $u_s(t)$ was measured using the granular PIV method with the high-speed video camera fixed normal to the flow surface. Figure 3 gives the change over time of the thickness h (thick dashed lines) and the surface velocity u_s (solid lines) for three slope inclinations: θ =21°, 27° and 33°. The thickness and the velocity are normalized by the particle diameter d and the typical velocity $\sqrt{gd}$ (based on the particle diameter), respectively. Curves highlight that the time t_i to reach the location x_0/d where the measurements are made decreases, not surprisingly, when the slope angle is decreased. Three avalanche phases characterizing the time-varying phenomenon are generally evidenced: (i) an increase in h and u_s, (ii) a maximum or even a plateau, and (iii) a more or less rapid decrease of h and u_s. Both the jamming transition at $\theta = \theta_{min}$ and the dense-to-dilute transition around $\theta = \theta_{max}$ were evidenced from these measurements on control avalanche flows: see details in [27]. Analysing in detail the experimental h and u_s data is beyond the scope of the present paper. These data will be used as an input for the model's equations presented in Sec.3.

In the second step, a wall of height $H = 25d$ spanning the whole width of the channel was placed at the channel exit. The time-varying normal force $F(t)$ exerted on the wall was measured with two $XFTC300$ piezoelectric sensors measuring the tension value at a

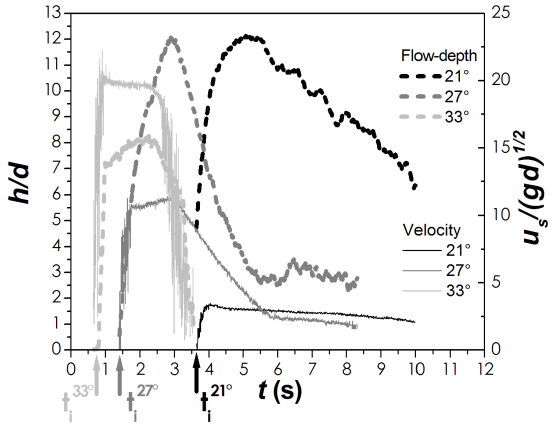

FIG. 3: Laboratory tests. Normalized thickness h/d (thick dashed lines) and surface velocity $u_s/\sqrt{gd}$ (solid lines) of the granular avalanches versus time t for three slope inclinations: θ =21° (black color), 27° (gray) and 33° (light gray).

frequency of 1 kHz. A specific sensor calibration (tension-force relation) as well as validation procedures (based on various known masses applied on different positions along the obstacle) were designed to ensure the accuracy of the force measurement (see details in [27]). Note that only the ten central centimeters, over the 25-cm width of the channel, were connected to force sensors in order to avoid resonance phenomena, as is shown in inset of Fig.2. Figure 4 provides the measured force per unit width, F/ℓ, on the wall for three slope inclinations: θ =21°, 27° and 33°. ℓ corresponds to the width of the part of the wall connected to the force sensors ($\ell = 100d$). Again, ones can observe that the time t_i to reach the obstacle decreases when the slope angle is decreased. Force signals also show the three avalanche phases characterizing the time-varying phenomenon: (i) an increase in force, (ii) a maximum in force or even a plateau, and (iii) a more or less rapid decrease of the force. More experimental data about the force are presented elsewhere [27] and in Sec.4 when these data are compared to the prediction of the analytical model described in Sec.3.

The changes over time (i) in thickness and velocity for control flows and (ii) in force are described and analysed in detail in [27]. The present paper focuses on the cross-comparison between the laboratory data and the analytical model recently proposed to describe the force from granular avalanches on the wall when a stagnant zone co-exists with a flowing zone above [21]. The model's equations to link the force to incoming flow depth and velocity are presented in the following section.

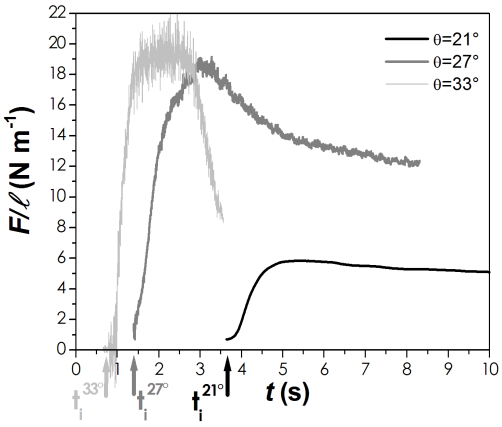

FIG. 4: Laboratory tests. Force per unit width, F/ℓ, measured on the wall versus time t for three slope inclinations: θ =21° (black color), 27° (gray) and 33° (light gray).

3. THEORETICAL FRAMEWORK

3.1. Depth-averaged momentum conservation

The following is a succinct description of the theoretical framework. Further details can be found in previous studies [20, 21]. Figure 1 gives a sketch of the flow geometry upstream of the obstacle. We define V_0 as the upstream volume disturbed by the obstacle. V_0 includes the volumes of the stagnant zone and of the flowing zone above (see hatched zone in Fig.1). Depth-averaged momentum conservation applied to V_0 leads to (see details in [20, 21]):

$$F = F_u^N + F_h + F_w^N - \bar{\mu}_{zm}\left[F_w^T + F_u^T\right] + F_{mv}, \tag{1a}$$

$$F_u^N/\ell_c = \beta\bar{\phi}\rho_P\bar{u}^2 h[1 - \delta_u \cos\alpha], \tag{1b}$$

$$F_h/\ell_c = \frac{1}{2}k\bar{\phi}\rho_P g h^2 \cos\theta, \tag{1c}$$

$$F_w^N/\ell_c = \bar{\phi}_0\rho_P\frac{V_0}{\ell_c}g\sin\theta, \tag{1d}$$

$$F_w^T/\ell_c = \bar{\phi}_0\rho_P\frac{V_0}{\ell_c}g\cos\theta, \tag{1e}$$

$$F_u^T/\ell_c = -\beta\bar{\phi}\rho_P\bar{u}^2 h\delta_u \sin\alpha, \tag{1f}$$

$$F_{mv}/\ell_c = -\frac{1}{2}\frac{d}{dt}\left[\bar{\rho}\bar{u}(1+\delta_u)\right], \tag{1g}$$

where F is the total normal force on the wall and ℓ_c is the channel width, which has to be

taken into account here contrary to two dimensional DEM simulations reported in [21]. h, $\bar{u}$ and $\bar{\phi}$ are, respectively, the flow thickness, the depth-averaged velocity and volume fraction at section S (see Fig.1). Eq.(1b) defines F_u^N which is the normal component of the force due to momentum variation between sections S and S^*. In order to derive F_u^N, we defined: the Boussinesq coefficient β related to the velocity profile in depth, the deflection angle α with respect to the flow bottom and the velocity ratio $\delta_u = \bar{u}^*/\bar{u}$, where $\bar{u}^*$ is the depth-averaged velocity at section S^*. Eq.(1c) gives F_h which is the pressure force of the incoming flow. k is classically defined as the earth's pressure coefficient [28]. F_w^N is the normal component of the weight of the control volume V_0. $\bar{\phi}_0 \rho_P V_0$, in Eq.(1d), is the mean mass of the control volume assumed to be equal to:

$$\bar{\phi}\rho_P \left(V_0 - \frac{1}{2} HL\ell_c \right) + \frac{1}{2}\phi_{max}\rho_P HL\ell_c, \tag{2}$$

in order to consider the compaction of the stagnant zone with respect to the flowing zone above. It is assumed that the dead zone has a triangular shape and L is its length (see Fig.1). ϕ_{max} is defined hereafter. The term $\bar{\mu}_{zm}\left[F_w^T + F_u^T\right]$ is the basal friction force between the dead zone and the rough bottom of the channel. It takes into account one contribution from the tangential component of the weight of the control volume (F_w^T) and another contribution from the tangential component of the force due to momentum variation between sections S and S^* (F_u^T). $\bar{\mu}_{zm}$ is the space-averaged coefficient of effective friction between the stagnant zone and the bottom (see detail in [20, 21] and in Sec.3.2). F_{mv} is the force due to momentum variation over time inside the control volume ($F_{mv} = 0$ in steady regime [20]). Detailed calculation to obtain Eq.(1g) is given in [21] based on the main assumption that the mean density and velocity are equal to $\bar{\phi}\rho_P$ and $\frac{1}{2}(\bar{u}+\bar{u}^*)$, in the volume $V_0 - \frac{1}{2}HL\ell_c$ (control volume V_0 minus the volume of the stagnant zone). The mass flux from the inertial zone to the quasi-static zone is neglected: we assume $\bar{\phi}^*\bar{u}^*h^* \simeq \bar{\phi}\bar{u}h$ for any time t, where $\bar{\phi}^*$ and h^* are volume fraction and thickness at section S^*. This assumption is reasonable except for times shorter than the characteristic time of the dead zone formation. The control volume V_0 is derived from geometry:

$$\frac{V_0}{\ell_c} = \frac{hL}{2}\left[2 + \left(\frac{L}{h} - \delta_h \sin\alpha \right) \tan\gamma + \frac{\delta_h}{L}(H-h)\sin\alpha \right], \tag{3}$$

where $\gamma = 2\alpha - \arctan\frac{H}{L}$ and $\delta_h = h^*/h$. The dead zone length is simply derived from

the triangular shape of the stagnant zone (see Fig.1):

$$L = \frac{H}{\tan(\alpha_{zm})}, \tag{4}$$

where α_{zm} is the dead zone angle (see Fig.1) and is defined in the next section. The jet angle with the channel bottom, or deflection angle, α is equal to the mean resulting value between the dead zone angle α_{zm} and the free-surface angle α_{sl} (see Fig.1):

$$\alpha = \frac{\alpha_{zm} + \alpha_{sl}}{2}. \tag{5}$$

3.2. Closure equations

The free-surface (α_{sl}) and dead zone (α_{zm}) angles are assumed to increase exponentially with time before reaching the asymptotic values α^0_{sl} and α^0_{sm} corresponding to the stationary state [20], as is proposed in [21]:

$$\alpha_{zm} = \alpha^0_{zm} + \left(\frac{\pi}{2} - \alpha^0_{zm}\right) e^{(t_i - t)/\tau}, \tag{6}$$

$$\alpha_{sl} = \alpha^0_{sl} + \left(\frac{\pi}{2} - \alpha^0_{sl}\right) e^{(t_i - t)/\tau}. \tag{7}$$

τ is the characteristic time of the stagnant zone formation and t_i depicts the measured time between the avalanche release and its first impact with the wall (see Figs.3 and 4). As we did not measure the growth of the dead zone in the laboratory experiments presented in this paper, we assume exponential variations similarly to what was observed for previous 2D DEM simulations (see figure 5 in [21]). Eqs.(6) and (7) are valid if $t \geqslant t_i$ otherwise $\alpha_{zm} = \alpha_{sl} = \pi/2$ when $t \leqslant t_i$. The asymptotic values α^0_{zm} and α^0_{sl} corresponding to a stationary state are derived using the results from previous 2D DEM simulations in steady regime (see detail in [20]):

$$\alpha^0_{zm} = \theta - \theta_{min}, \tag{8}$$

$$\alpha^0_{sl} = \frac{\theta_{min}}{\theta_{max} - \theta_{min}}(\theta - \theta_{min}), \tag{9}$$

In [20] where steady flows were studied thanks to discrete numerical simulations, it is shown that the angle of the dead zone with respect to the horizontal, equal to $\theta - \alpha^0_{zm}$, does

not depend on the slope angle and is equal to the constant value θ_{min}, which leads to Eq.(8). Equation 9 is derived from the fact that the free-surface angle in steady regime, α_{sl}^0, is a simple affine function of the slope angle θ: $\alpha_{sl}^0 = a\theta + b$, where a and b are calculated with the following physical arguments: (i) α_{sl}^0 tends towards zero when $\theta = \theta_{min}$ (the dead zone propagates increasingly upstream of the wall), which gives $\alpha_{sl}^0 = a(\theta - \theta_{min})$ and (ii) α_{sl}^0 tends towards θ_{min} when $\theta = \theta_{max}$ (the free-surface and the frontier between the stagnant zone and the flowing zone above are parallel), which gives $a = \theta_{min}/(\theta_{max} - \theta_{min})$. Here, for a sake of simplicity, we do not distinguish slopes below and above θ_{max} as it was proposed in [20, 21] where different values of a and b were given when $\theta > \theta_{max}$. We verified that this choice had very little effect on the model's prediction displayed in Sec.4.

Two other closure equations are needed to derive the velocity reduction δ_u and the basal friction coefficient $\bar{\mu}_{zm}$. The velocity reduction is calculated using the empirical relation proposed in [20] assuming that the relative velocity reduction is proportional to the deflecting –or jet– angle (the larger the deflecting angle α, the higher the expected velocity decrease is): $(\bar{u} - \bar{u}^*)/\bar{u} = \kappa\alpha$, which leads to

$$\delta_u = 1 - (1 - e)\frac{\alpha}{\pi/2} = \frac{1}{\delta_h}, \tag{10}$$

where e is the restitution coefficient of particles ($e \approx 0.9$ for glass beads) stemming from the limit condition corresponding to a purely collisional regime at high slope (jet angle equal to $\alpha = \pi/2$) for which $\delta_u \simeq e = 1 - \kappa\pi/2$. The depth variation $\delta_h = h^*/h$ is simply derived from mass conservation by assuming that the volume fraction is relatively unchanged between sections S and S^*. Finally, the basal friction coefficient is also derived from the results from previous discrete numerical simulations with the following relation compatible with the dead zone angle (see [20, 21]):

$$\bar{\mu}_{zm} = \tan(\theta - \alpha_{zm}). \tag{11}$$

Equations (1–11) can be used to predict the force on the wall if the time signals $h(t)$, $\bar{u}(t)$ and $\bar{\phi}(t)$ are known. The entire calculation to derive Eqs.(1–11) is detailed in [20] for the steady regime and in [21] for the time-varying avalanche regime. The following section deals with the cross-comparison between the laboratory data and the prediction from the set of Eqs.(1–11).

4. FORCE ON THE WALL: MODEL VERSUS LABORATORY TESTS

4.1. Model's parameters

Contrary to DEM simulations for which $h(t)$, $\bar{u}(t)$ and $\bar{\phi}(t)$ signals could be simultaneously measured for control flows [21], we only measured $h(t)$ and $u_s(t)$ here. We assume $u_s(t) \approx \bar{u}(t)$ and we estimate $\bar{\phi}$ with (see [18]):

$$\bar{\phi}(\bar{I}) = \phi_{max} + (\phi_{min} - \phi_{max})\bar{I}, \tag{12}$$

where ϕ_{min}=0.4 and ϕ_{max}=0.64 are typical minimum and maximum values of the volume fraction for relatively dense granular flows. $\bar{I}$ is the macroscopic inertial number [19]: $\bar{I} = 5\bar{u}d/2h\sqrt{gh\cos\theta}$. Eq.(12) is strictly valid for slopes in the range $[\theta_{min},\theta_{max}]$. For $\theta \geq \theta_{max}$, it gives unreasonable values. We found very low $\bar{\phi}$-values that were not compatible with the experimental observations, or even negative unphysical values, resulting from large $\bar{I}$ values (rapid and thin flows). This point is discussed below when cross-comparing the predicted force and the experimental data.

The following parameters are needed to derive the force from the model's equations presented in Sec.3: θ_{min}, θ_{max}, e, k, β, t_i and τ. The friction angles $\theta_{min} = 20°$ and $\theta_{max} = 28°$ were experimentally determined from the function $h_{stop}(\theta)$. The restitution coefficient of particles e was estimated to 0.9 for the glass beads used in the experiments. The model's sensitivity to the earth pressure coefficient k and to the Boussinesq coefficient β was found to be insignificant, as also reported in [21]: $k = 1$ and $\beta = 1$ were therefore chosen. t_i corresponds to the initial impact of the avalanche front with the wall. It was estimated from the measurements of thickness and velocity combined with force: see examples in Figs.3 and 4. As we did not measure the growth of the dead zone, the characteristic time related to the dead zone formation was firstly fixed at $\tau = 0.4$s for any slope on the basis of the DEM simulations reported in [21] for which the growth of the dead zone was analysed (see figure 5 in [21]). We are aware that the creation of the dead zone is a key point here. The dynamics of the dead zone should be studied in detail in the future in order to investigate the possible influence of parameters such as the obstacle and channel sizes on the characteristic time τ.

4.2. Model's prediction

Without any other fitting procedure, except the choice to discriminate between slopes above and below θ_{max} to calculate $\bar{\phi}$ [see discussion hereafter and Figs.6(a) and 6(b)], the model's prediction is found to be in quantitative agreement with the experimental data for a large range of slopes, as displayed in Fig.5(a). For slopes close to θ_{min} ($\theta \leq 24°$), it was necessary to increase τ above the initial value of 0.4s mentioned in previous section [see also discussion hereafter and Fig.5(b)]. The analytical model is able to reproduce the different phases of the avalanche for a certain range of slope angles: (i) the increase in force, (ii) the maximum in force, or even the plateau, and (iii) the force decrease. For $\theta \geq 27°$ (close to θ_{max}), preliminary tests showed that the model's prediction could give good results if the volume fraction was corrected with $\bar{\phi}(t) = \phi_{min}$ for any time instead of the time-varying values derived from $\bar{I}$. For $\theta \geq 27°$, the results can be improved using the volume fraction as a fitting parameter: the final results are illustrated in Fig.5(a).

Interestingly is the comparison of the obtained $\bar{\phi}$-values to previous existing experimental measures of volume fraction inside granular avalanches. Figure 6(a) gives the maximum value ϕ_M reached by the volume fraction [derived from $\bar{I}$ with the help of Eq.(12)] versus the slope as well as the fitted values ϕ_{fit} (constant value for any time) when $\theta \geq 27°$. The data are displayed in terms of $\bar{\phi}/\phi_{max}$ as a function of $\tan\theta/\tan\theta_{min}$ so that they can be compared to previous experimental data from figure 15 in [29]. The fitted values ϕ_{fit} (for $\theta \geq 27°$) are compatible with the laboratory data from [29], whereas the values derived from the $\bar{\phi}(\bar{I})$ relation [Eq.(12)] are systematically lower when $\theta \geq 27°$. This result confirms that the $\bar{\phi}(\bar{I})$-relation is no longer valid above a critical angle close to θ_{max}. Fig.6(b) shows the increase of the difference $\phi_{fit} - \phi_M$ with slope (we consider that $\phi_{fit} = \phi_M$ for $\theta \leq 27°$ in absence of fitting procedure), which can be seen as the trace of the dense-to-dilute transition in gravity-driven granular flows at slope angle θ close to θ_{max} [18]. As we did not measure the volume fraction in the presented laboratory tests, we are not able to conclude whether such a transition in volume fraction really occurs in the experiments or not. It may be only an artefact of the fitting procedure on $\bar{\phi}$. Future experiments including measurements of the volume fraction, based on indirect and cost-effective methods applied to gravity-driven granular flows [29, 30] (compared to the existing sophisticated magnetic resonance imaging or the radioactive positron emission particle tracking methods), would be of great interest

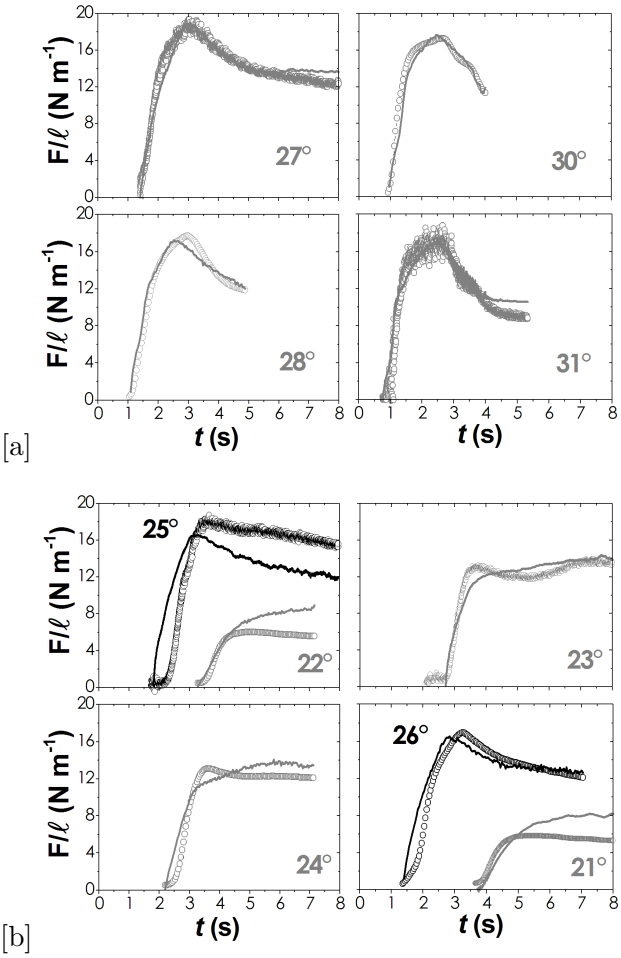

FIG. 5: Normal force per unit of width F/ℓ (N m^{-1}) versus time t (s): cross-comparison between the model's prediction from Eqs. (1–11) (lines) and the experimental data (circles). (a) Model predictions are shown with $\bar{\phi} = \phi_{fit}$ [see Fig.6(b)]. (b) Model predictions are shown with a fitted value of τ [see Fig.6(c)] for $\theta \leq 24°$.

to verify this point.

It is worth mentioning that for the lowest θ (nearby θ_{min}) the model failed: it overestimated strongly the force $F(t)$ with $\tau = 0.4$ s. The gap between the model and experimental data could be reduced by using τ as a fitting parameter for slopes smaller than $\theta = 24°$. Fig.6(c) displays the characteristic time τ stemming from this fitting procedure. τ increases when approaching θ_{min}, which is compatible with the expectation that the dead zone would indefinitely propagate upstream of the wall for $\theta = \theta_{min}$. In Fig.5(b) are shown the results with the fitted values of τ for $\theta \leq 24°$. The agreement is still not perfect contrary to 2D DEM simulations [21]. This can be explained by the possible effects related to the jamming

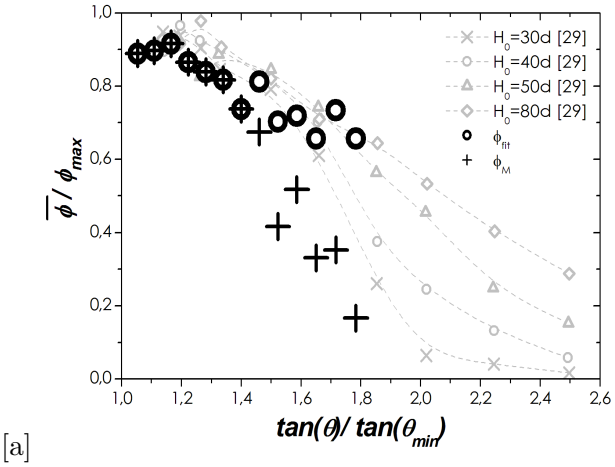

[a]

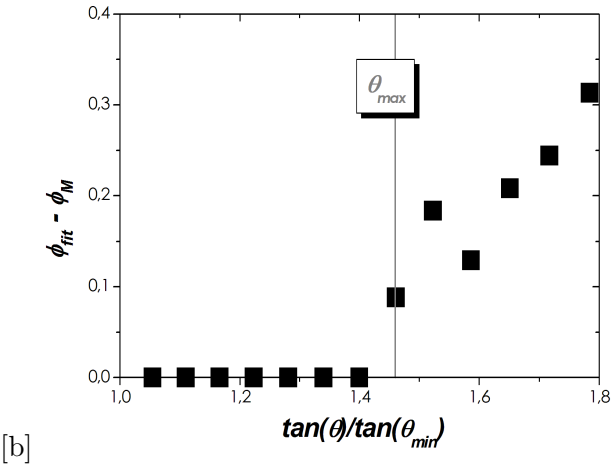

[b]

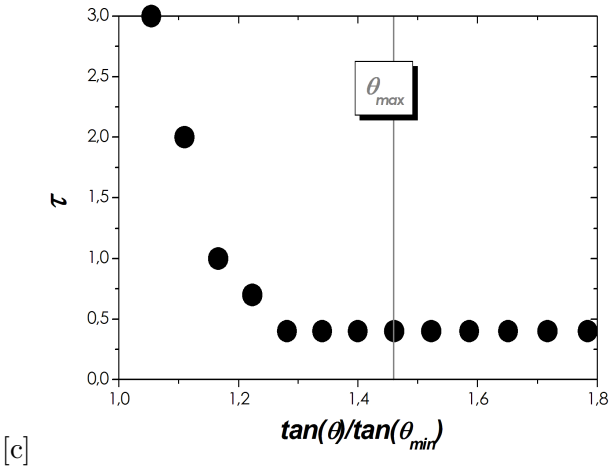

[c]

FIG. 6: (a) Normalized volume fraction $\bar{\phi}/\phi_{max}$ versus $\tan\theta/\tan\theta_{min}$: maximum values ϕ_M derived from $\bar{I}$, via Eq.(12) (cross symbols) and fitted values ϕ_{fit} with $\phi_{fit} = \phi_M$ for $\theta \leq 27°$ (circles); the values measured in [29] are also given for comparison (gray symbols). (b) Difference $\phi_{fit} - \phi_M$ versus $\tan\theta/\tan\theta_{min}$ (we consider that $\phi_{fit} - \phi_M = 0$ for $\theta < 27°$ in absence of fitting procedure). (c) Characteristic time τ versus $\tan\theta/\tan\theta_{min}$ ($\tau = 0.4$s for $\theta \geq 25°$). The vertical dashed lines in graphs (b) and (c) correspond to $\theta = \theta_{max}$.

transition that are not considered in the proposed model (forces per unit of width), which can increase the friction term (resulting in F decrease): (i) wall effects related to the formation of a network of strong force chains and (ii) the fact that the flow started to come to a standstill before reaching the wall with no –or slight– overflow. By construction, the first effect does not exist in the 2D DEM simulations reported in [21]. The second effect is enhanced in the laboratory tests for which the wall was placed at a distance x_0/d =1300, much greater than x_0/d=500 for the 2D DEM simulations in [21]. Investigating the influence of the channel and the obstacle sizes on these effects –in link with a kind of dynamic Janssen effect– is beyond the scope of this paper but would be of crucial interest in the future.

The results for $\theta = 29°$, $32°$ and $33°$, not shown here, are fully compatible with the results illustrated in Fig.5(a). The results are presented with $F_{mv} = 0$ in Fig.5 because this term was shown to have a negligible influence on the model's prediction, as also found for DEM simulations in [21].

Beyond its ability to predict the measured time-varying force on the wall, the analytical model gives the various contributions to the total force F, which provides a better understanding of the avalanche–wall interaction over time. Figure 7 gives an example for $\theta = 31°$. The inertial force F_u^N related to the square of the incoming velocity and taking into account the velocity reduction [Eq.(1b)], decreases substantially from $t = 1.25$s to $t = 3$s (dark gray line in Fig.7), whereas the apparent weight, $F_w^N - \bar{\mu}_{zm}(F_w^T + F_u^T)$, of the upstream volume disturbed by the wall becomes equal to F_u^N at $t = 1.25$s and increases to reach a maximum at around $t = 2.5$s. Note that the pressure force F_h from the incoming flow remains negligible at any time of the flow-obstacle interaction here. Fig.7 generally emphasizes the strong contribution stemming from the dead zone process occurring upstream of the wall.

5. DISCUSSION AND CONCLUSION

Importantly is the maximum pressure experienced by the wall that can be compared to typical pressures related to the control flow without any obstacle. Fig.8(a) reports the maximum pressures $P_{max} = F_{max}/(\ell H)$ scaled by the typical pressures $P_0 = F_0/(\ell_c h_m)$ of the incident control flows versus the scaled slope $\tan\theta/\tan\theta_{max}$, with $F_0 = F_h^0 = 1/2\bar{\phi}\rho_P {h_m}^2 \ell_c \cos\theta$ (pressure force) or $F_0 = F_u^0 = 1/2\bar{\phi}\rho_P {u_m}^2 h_m \ell_c$ (kinetic force). h_m is the maximum thickness of the control flows and u_m the related velocity. At high values for θ, Fig.8(a) shows that

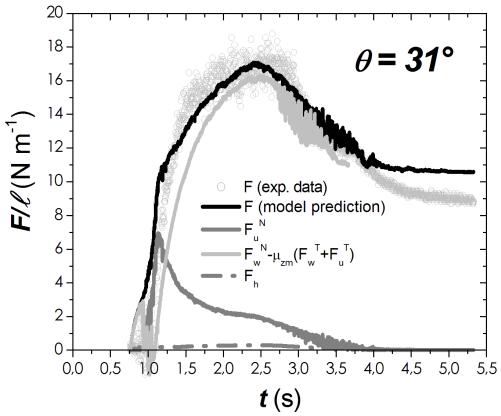

FIG. 7: Normal force per unit of width versus time (example for $\theta = 31°$). The various contributions [Eq.(1a)] to the total force (black line) are shown: normal inertial force F_u^N (dark gray line), pressure force F_h (dark gray dashed line) and apparent weight $F_w^N - \bar{\mu}_{zm}(F_w^T + F_u^T)$ (light gray line). The force due to momentum variation over time, F_{mv}, is not shown (this is negligible for any slope, as found in [21]).

the maximum force is driven by inertia: P_{max}/P_u^0 is relatively constant. At low slopes, the ratio P_{max}/P_h^0 ranges from 10 (around θ_{max}) to 3 (close to θ_{min}). This result is caused by the additional and dominant contribution of the apparent weight of the upstream volume disturbed by the wall. These curves are fully compatible with the laboratory results from 2D DEM simulations reported ealier in [20, 21] and drawn in Fig.8(b). It can be concluded that the maximum pressures from both the DEM simulations (purely 2D) and the laboratory tests (channelized flows) are well reproduced by the analytical model, which is able to catch the transition in force at the slope angle θ close to θ_{max}.

In conclusion, we have carried out laboratory tests on confined granular avalanche overflowing a wall. 2D DEM numerical simulations were previously reported in [21], which allowed to develop and calibrate an equation to predict the avalanche force in similar flow–obstacle configuration. Up to now, no experimental verification of the model has been available. Except for low slopes, the equation was successfully compared to the laboratory data, which demonstrates the robustness of the force model. Morever, it confirms that the force experienced by the wall overflowed by a granular avalanche is the sum of (i) the pressure force of the incoming undisturbed flow, (ii) the inertial force related to velocity reduction and (iii) the apparent weight of the upstream volume –the quasistatic zone sur-

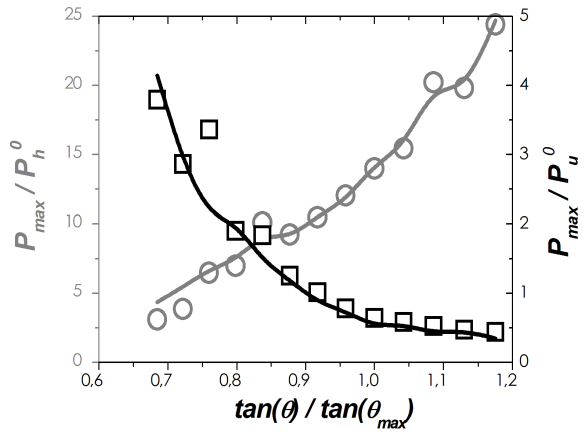

[a]

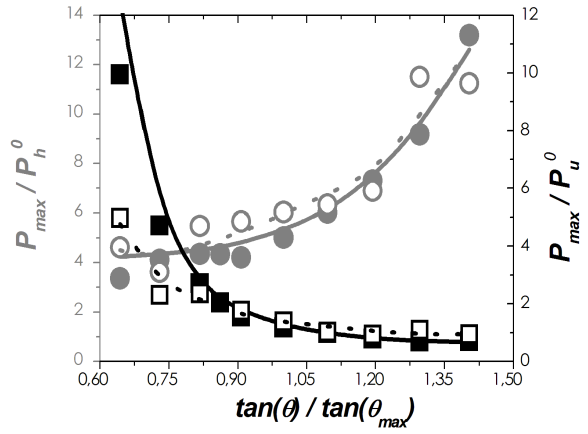

[b]

FIG. 8: Maximum pressure $P_{max} = F_{max}/(\ell H)$ scaled by pressures $P_0 = F_0/(\ell_c h_m)$ with $F_0 = 1/2\bar{\phi}\rho_P {h_m}^2 \ell_c \cos\theta$ (pressure force, circles and lines in gray) or $F_0 = 1/2\bar{\phi}\rho_P {u_m}^2 h_m \ell_c$ (kinetic force, squares and lines in black) versus the scaled slope $\tan\theta/\tan\theta_{max}$: (a) model's prediction (lines) compared to experimental data (symbols); (b) model's prediction (lines) compared to DEM simulations in steady (plain symbols and solid lines, [20]) and avalanche (empty symbols and dotted lines, [21]) regimes.

mounted by the inertial zone– disturbed by the obstacle. The proposed equations based on depth-averaged momentum equations are sufficient to link the growth of the dead zone to the mean force. However, it is worthy of pointing at that the granular temperature goes to zero in the quasi-static stagnant zone and the related dissipation must be very important. Hence, this description may fail to describe the creation of the dead zone and the force fluctuations on the wall. Investigating the physical process at a microscopic (grain) scale is a futur challenge. Finally, quantifying the gap between the laboratory data and the equation at the

lowest slopes, attributed to wall effects occurring near the jamming transition, remains an important challenge. Laboratory tests and/or 3D DEM simulations with various channel width and obstacle height should be undertaken in the future to verify these assumptions in link with a Janssen effect. It will also provide crucial information on the characteristic time defining the growth of the dead zone when the obstacle and the channel sizes are varied.

Acknowledgments

We would like to thank H. Bellot and F. Ousset for great help with the experiments. We also thank Mohamed Naaim and Yoël Forterre for fruitful discussions. We gratefully acknowledge research support from the following projects: DynAval (Interreg Alcotra), MONHA (ANR) and MOPERA (ANR).

[1] U. Tuzun, and R.M. Nedderman, Chem. Eng. Sci. **40**, 337 (1985).

[2] X. Cui, J.M.N.T. Gray, and T. Johannesson, J. Geophys. Res. **112**, F04012 (2007).

[3] T. Faug, P. Gauer, K. Lied, and M. Naaim, J. Geophys. Res. **113**, F03009 (2008).

[4] K. Wieghardt, Ann. Rev. Fluid. Mech. **7**, 89 (1975).

[5] R. Albert, M.A. Pfeifer, A.-L. Barabasi, and P. Schiffer, Phys. Rev. Lett. **82**, 205 (1999).

[6] I. Albert, P. Tegzes, B. Kahng, R. Albert, J.G. Sample, M. Pfeifer, A.-L. Barabasi, T. Vicsek, and P. Schiffer, Phys. Rev. Lett. **84**, 5122 (2000).

[7] I. Albert, J.G. Sample, A.J. Morss, S. Rajagopalan, A.-L. Barabasi, P. Schiffer, Phys. Rev. E **64**, 061303 (2001).

[8] D. Chehata, R. Zenit, and C.R. Wassgren, Phys. Fluids **15** (6), 1622-1631 (2003).

[9] G. Hill, S. Yeung, and S.A. Koehler, Europhys. Lett. **72** (1), 137 (2005).

[10] V. Buchholtz and T. Poschel, Granular Matter **1** (1998).

[11] E.C. Rericha, C. Bizon, M.D. Shattuck, and H.L. Swinney, Phys. Rev. Lett. **88**, 014302 (2001).

[12] C.R. Wassgren, J.A. Cordova, R. Zenit, and A. Karion, Phys. Fluids **15** (11), 3318-3330 (2003).

[13] R. Bharadwaj, C. Wassgren, and R. Zenit, Phys. fluids **18** (4), 043301 (2006).

[14] A. Levy and M. Sayed, Phys. Fluids **19** (2), 023302 (2007).

[15] A. Levy and M. Sayed, Powder Tech. **181** (2), 137-148 (2008).

[16] J. F. Boudet and H. Kellay, Phys. Rev. Lett. **105**, 104501 (2010).

[17] H.M. Jaeger, S.R. Nagel, and R.P. Behringer, Rev. Mod. Phys. **68**, 1259 (1996).

[18] Y. Forterre and O. Pouliquen, Ann. Rev. Fluid. Mech. **40**, 1 (2008).

[19] GDR Midi, E. Phys. J.E **14**, 341 (2004).

[20] T. Faug, R. Beguin, and B. Chanut, Phys. Rev. E **80**, 021305 (2009).

[21] B. Chanut, T. Faug, and M. Naaim, Phys. Rev. E **82**, 041302 (2010).

[22] C.E. Brennen, K. Sieck, and J. Paslaski, Powder Tech. **35**, 31 (1983).

[23] S.B. Savage, J. Fluid Mech. **92**, 53 (1979).

[24] S. P. Pudasaini, K. Hutter, S. S. Hsiau, S. C. Tai, Y. Wang, and R. Katzenbach, Phys. Fluids **19**, 053302 (2007).

[25] S. P. Pudasaini and C. Kroner, Phys. Rev. E **78**, 041308 (2008).

[26] O. Pouliquen, Phys. Fluids **11** (3), 542 (1999).

[27] P. Caccamo, B. Chanut, T. Faug, H. Bellot, and F. Naaim-Bouvet, submitted to Granular Matter.

[28] S.B. Savage and K. Hutter, J. Fluid Mech. **199**, 177-215 (1989).

[29] T. Börzsönyi, R.E. Ecke, Phys. Rev. E **74**, 061301 (2006).

[30] L.T. Sheng, C.Y. Kuo, Y.C. Tai, S.S. Hsiau, Exp. Fluids (2011) doi:10.1007/s00348-011-1149-4.